Conference Proceedings of the Society for Experimental Mechanics Series

Robert Barthorpe · Roland Platz · Israel Lopez
Babak Moaveni · Costas Papadimitriou *Editors*

Model Validation and Uncertainty Quantification, Volume 3

Proceedings of the 35th IMAC, A Conference and Exposition on Structural Dynamics 2017

Springer

Conference Proceedings of the Society for Experimental Mechanics Series

Series Editor

Kristin B. Zimmerman, Ph.D.
Society for Experimental Mechanics, Inc.,
Bethel, CT, USA

More information about this series at http://www.springer.com/series/8922

Robert Barthorpe • Roland Platz • Israel Lopez • Babak Moaveni
Costas Papadimitriou
Editors

Model Validation and Uncertainty Quantification, Volume 3

Proceedings of the 35th IMAC, A Conference and Exposition on Structural Dynamics 2017

Springer

Editors
Robert Barthorpe
University of Sheffield
Sheffield, UK

Israel Lopez
Lawrence Livermore National Laboratory
Livermore, CA, USA

Costas Papadimitriou
University of Thessaly
Thessaly, Greece

Roland Platz
Fraunhofer Institute Darmstadt
Darmstadt, Germany

Babak Moaveni
Tufts University
Medford, MA, USA

ISSN 2191-5644 ISSN 2191-5652 (electronic)
Conference Proceedings of the Society for Experimental Mechanics Series
ISBN 978-3-319-54857-9 ISBN 978-3-319-54858-6 (eBook)
DOI 10.1007/978-3-319-54858-6

Library of Congress Control Number: 2017943322

Printed on acid-free paper

This Springer imprint is published by Springer Nature
The registered company is Springer International Publishing AG
The registered company address is: Gewerbestrasse 11, 6330 Cham, Switzerland

Preface

Model Validation and Uncertainty Quantification represents one of ten volumes of technical papers presented at the 35th IMAC, A Conference and Exposition on Structural Dynamics, organized by the Society for Experimental Mechanics and held in Garden Grove, California, on January 30–February 2, 2017. The full proceedings also include the following volumes: Nonlinear Dynamics; Dynamics of Civil Structures; Dynamics of Coupled Structures; Sensors and Instrumentation; Special Topics in Structural Dynamics; Structural Health Monitoring & Damage Detection; Rotating Machinery, Hybrid Test Methods, Vibro-Acoustics and Laser Vibrometry; Shock & Vibration, Aircraft/Aerospace, and Energy Harvesting; and Topics in Modal Analysis & Testing.

Each collection presents early findings from experimental and computational investigations on an important area within structural dynamics. Model Validation and Uncertainty Quantification (MVUQ) is one of these areas.

Modeling and simulation are routinely implemented to predict the behavior of complex dynamical systems. These tools powerfully unite theoretical foundations, numerical models, and experimental data which include associated uncertainties and errors. The field of MVUQ research entails the development of methods and metrics to test model prediction accuracy and robustness while considering all relevant sources of uncertainties and errors through systematic comparisons against experimental observations.

The organizers would like to thank the authors, presenters, session organizers, and session chairs for their participation in this track.

Sheffield, UK — Robert Barthorpe
Darmstadt, Germany — Roland Platz
Livermore, CA, USA — Israel Lopez
Medford, MA, USA — Babak Moaveni
Thessaly, Greece — Costas Papadimitriou

Contents

Chapter 1
Lateral Vibration Attenuation of a Beam with Piezo-Elastic Supports Subject to Varying Axial Tensile and Compressive Loads

Benedict Götz, Roland Platz, and Tobias Melz

Abstract In this paper, vibration attenuation of a beam with circular cross-section by resonantly shunted piezo-elastic supports is experimentally investigated for varying axial tensile and compressive beam loads. Varying axial beam loads manipulate the effective lateral bending stiffness and, thus, lead to a detuning of the beams resonance frequencies. Furthermore, varying axial loads affect the general electromechanical coupling coefficient of transducer and beam, an important modal quantity for shunt-damping. The beam's first mode resonance frequency and coupling coefficient are analyzed for varying axial loads. The values of the resonance frequency and the coupling coefficient are obtained from a transducer impedance measurement. Finally, frequency transfer functions of the beam with one piezo-elastic support either shunted to a RL-shunt or to a RL-shunt with negative capacitance, the RLC-shunt, are compared for varying axial loads. It is shown that the beam vibration attenuation with the RLC-shunt is less influenced by varying axial beam loads.

Keywords Piezo-elastic support • Resonant shunt • Vibration attenuation • Beam • Axial load

1.1 Introduction

Structural vibration may occur in mechanical systems leading to fatigue, reduced durability or undesirable noise. In this context, resonant shunting of piezoelectric transducers can be an appropriate measure for attenuating vibrations. Shunt-damping in general has been subject to research for several decades [1] and resulted in many diverse shunt concepts such as mono- or multi-modal resonant shunts [2], shunts with negative capacitances [3] or switched shunts [4]. Shunting a piezoelectric transducer with resistor and inductance, the RL-shunt, a tuned electrical oscillation circuit with the inherent capacitance of the transducer is created. This electromechanical system acts similar to a mechanical vibration absorber. RL-shunts are easy to implement and no stability limits or switching laws have to be taken into account. However, the achieved vibration attenuation significantly depends on the tuning of the shunt parameters and the amount of the general electromechanical coupling coefficient of transducer and structure [5]. By adding a negative capacitance, the RLC-shunt achieves higher vibration attenuation but stability issues have to be considered.

In mechanical and civil engineering, truss structures bear and withstand constant and variable loads that may lead to vibrations. Truss structures comprise truss members such as beams that are connected to each other via the relatively stiff truss supports. On the one hand, truss structures show global vibration modes with lateral moving or rotating truss supports. On the other hand, local modes exist that are dominated by the lateral vibration behavior of each beam. Additional varying quasi static loading may result in axial tensile and compressive loads of the beams. This affects the resulting lateral bending stiffness of the beams leading to a permanent change in the resonance frequencies. For vibration attenuation with resonant shunt-damping, the detuning of the resonance frequencies affects the achievable vibration attenuation capability. In truss structures, piezoelectric shunt-damping has been investigated in [6–8]. Axial piezoelectric stack transducers are integrated within one strut of the truss, resulting in compression and elongation of the transducer in normal axial direction of the strut [6, 8]. In [7], a beam support with integrated piezoelectric washers alongside the beam that are strained in shear under dynamic loading has been investigated and vibration attenuation of bending modes in a truss substructure was achieved. Due to a planar washer design, only one bending direction of the beams could be influenced. Nevertheless, research

B. Götz (✉) • T. Melz
System Reliability, Adaptive Structures, and Machine Acoustics SAM, Technische Universität Darmstadt, Magdalenenstraße 4, 64289 Darmstadt, Germany
e-mail: goetz@sam.tu-darmstadt.de

R. Platz
Fraunhofer Institute for Structural Durability and System Reliability LBF, Bartningstraße 47, 64289 Darmstadt, Germany

R. Barthorpe et al. (eds.), *Model Validation and Uncertainty Quantification, Volume 3*,
Conference Proceedings of the Society for Experimental Mechanics Series, DOI 10.1007/978-3-319-54858-6_1

investigating the effect of varying quasi static axial beam loads on the vibration attenuation of beams with resonant shunt-damping are not known to the authors.

In this paper, a new concept of a piezo-elastic support [9] for vibration attenuation of truss structures comprising beams with circular cross-section by shunted transducers is investigated for varying axial tensile and compressive beam loads. Within the piezo-elastic support, deflections in both lateral directions of a beam are transferred into an axial deformation of the transducers that are arranged perpendicular to one free end of the beam. By that design, local and global truss modes can attenuated without manipulating the beam's surface. In the following only one beam with two piezo-elastic supports is investigated for varying axial tensile and compressive loads. One piezo-elastic support mechanically excites the beam laterally using white noise excitation while the second support is either shunted to a RL- or to a RLC-shunt. First, the experimental beam's first mode resonance frequency and its general electromechanical coupling coefficient are calculated from impedance measurements for different axial tensile and compressive loads. Changes in both, the resonance frequency and the coupling coefficient may influence the vibration attenuation. Considering the electrical transducer impedance in the frequency domain is a known method for identifying the transducer capacitance, structural resonance frequencies or the coupling coefficient and has several advantages. E.g., all important quantities are obtained from one measurement at one time, no structural transfer function has to be measured and the estimation of the resonance frequency as well as the coupling coefficient is less influenced by the used frequency resolution [10]. Second, the experimental frequency transfer functions in lateral direction of the excited beam in case one transducer is shunted to a RL-shunt and in case one transducer is shunted to a RLC-shunt are compared for uncertain axial tensile and compressive beam loads.

1.2 System Description

The investigated system is a beam under axial load made of aluminum alloy EN AW-7075 with length $l_\mathrm{b} = 400\,\mathrm{mm}$ and circular solid cross-section of radius $r_\mathrm{b} = 5\,\mathrm{mm}$, Fig. 1.1. The circumferential lateral stiffness is homogeneous and has no preferred direction of lateral deflection, so the beam may vibrate in any plane lateral to the longitudinal x-axis. The beam is supported by two piezo-elastic supports A and B at location $x = 0$ and location $x = l_\mathrm{b}$. Elastic membrane-like spring elements made of spring steel 1.1248 in both supports A and B at location $x = 0$ and $x = l_\mathrm{b}$ bear axial and lateral forces at the beam's ends in x-, y- and z-direction, and allow rotation φ_y and φ_z in any plane perpendicular to the x-axis, see Fig. 1.2. In Fig. 1.1, the membrane-like spring elements for both supports A and B are represented by axial stiffness $k_{x,\mathrm{A}} = k_{x,\mathrm{B}} = 1.53 \times 10^4\,\mathrm{N/mm}$, not shown in the figure, lateral stiffness $k_{y,\mathrm{A}} = k_{z,\mathrm{A}} = k_{y,\mathrm{B}} = k_{z,\mathrm{B}} = k_\mathrm{l} = 9.98 \times 10^4\,\mathrm{N/mm}$ in y- and z-direction and rotational stiffness $k_{\varphi_y,\mathrm{A}} = k_{\varphi_z,\mathrm{A}} = k_{\varphi_y,\mathrm{B}} = k_{\varphi_z,\mathrm{B}} = k_\mathrm{r} = 2.69 \times 10^5\,\mathrm{N\,mm/rad}$ around the y- and z-axes. All spring element stiffness values are obtained from a finite element simulation and they are not experimentally verified yet. In each piezo-elastic support A and B at $x = -l_\mathrm{ext}$ and $x = l_\mathrm{b} + l_\mathrm{ext}$, two piezoelectric stack transducers P_1 and P_2 as well as P_3 and P_4 are arranged in the support housing at an angle of 90° to each other orthogonal to the beam's x-axis, Fig. 1.1b. All transducers are mechanically prestressed by a stack of disc springs with stiffness $k_\mathrm{pre} = 2.6 \times 10^3\,\mathrm{N/mm}$. The transducers are connected to the beam via a relatively stiff axial extension made of hardened steel 1.2312 with length $l_\mathrm{ext} = 6.75\,\mathrm{mm}$ and edge length $t_\mathrm{ext} = 12\,\mathrm{mm}$. With that, lateral beam deflections in y- and z-direction due to vibration excitation are transformed into the stack transducer's axial deformation. Each piezoelectric transducer $\mathrm{P_1}$ to $\mathrm{P_4}$ is a PI P-885.51 stack transducers with the capacitance $C_\mathrm{p} = 1.65\,\mu\mathrm{F}$ at constant mechanical stress, internal series resistance $R_\mathrm{p} = 7\,\Omega$ and the mechanical stiffness $k_\mathrm{p} = 50 \times 10^3\,\mathrm{N/mm}$ with short circuited electrodes, defined as the ratio of the transducer's block force and the maximum free stroke. The input current to the transducer is $I(t)$ and the potential difference at the transducer electrodes is the voltage $U(t)$.

For vibration attenuation, a RL- and a RL-shunt with negative capacitance C, the RLC-shunt, are taken into account, Fig. 1.1c. In Fig. 1.1c, the RL-shunt is obtained by neglecting the negative capacitance. By adjusting the inductance L and the damping resistance R, the transducer shunted to a RL-shunt attenuates vibrations similar to a mechanical vibration absorber [1]. For vibration attenuation with shunt-damping, the generalized electromechanical coupling coefficient K_{33} is an important modal quantity indicating the vibration attenuation capability. The higher the value of K_{33} is, the higher the achievable vibration attenuation with a RL-shunt becomes. By adding a negative capacitance $C \approx -1.02 \cdot C_\mathrm{p}$ in series to R and L, the coupling coefficient K_{33} increases effectively and, hence, the vibration attenuation capability is significantly higher compared to the simple RL-shunt [5]. Apart from that, RLC-shunts may destabilize the beam vibration, therefore, stability limits for the value of C have to be considered. Basically, the achievable vibration attenuation capability with a RLC-shunt is almost independent of the coupling coefficient K_{33}. However, the smaller the coupling coefficient is, the close the value of the negative capacitance has to be chosen to the stability limit [5]. In the experiment, the inductance L is implemented by the use of a gyrator circuit and the negative capacitance by the use of negative admittance converter [2]. Both circuit designs are not discussed in detail in this paper.

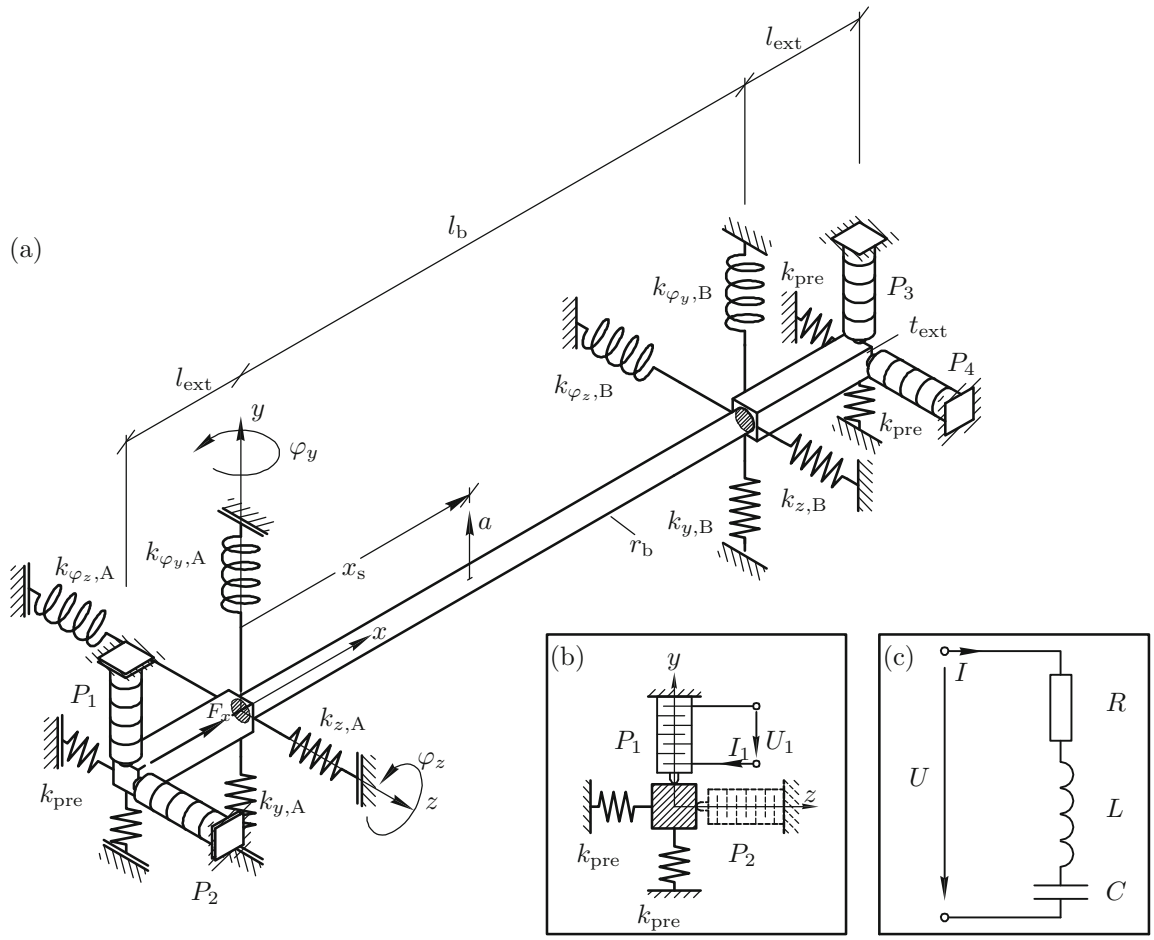

Fig. 1.1 Beam system, (**a**) beam with piezo-elastic supports A and B, (**b**) arrangement of piezoelectric transducers, (**c**) shunt circuit

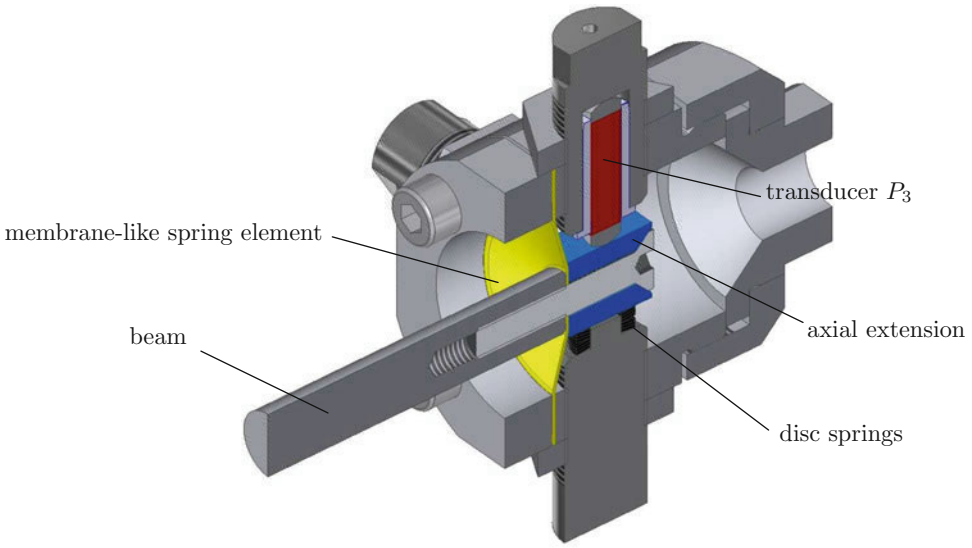

Fig. 1.2 Sectional view of piezo-elastic support [11]

For all experimental vibration attenuation investigations, the piezoelectric transducer P_1 excites the beam in y-direction via a controlled voltage signal $U_1(t)$. The transducer P_3, either shunted to the RL-shunt or the RLC-shunt, attenuates the vibration acceleration $a(t)$ at the sensor location x_s while the transducers P_2 and P_4 are operated with short circuited (sc) electrodes. Varying axial tensile and compressive loads $-1000\,\mathrm{N} \leq F_x \geq 1500\,\mathrm{N}$, with compressive loads in positive x-direction, are applied to the beam at $x = 0$ via a spindle-type lifting gear and measured by a force sensor.

1.3 The Beam's First Mode Eigenfrequency and Coupling Coefficient for Varying Axial Loads

The vibration attenuation capability bears on the piezoelectric transducers P_3 that is either shunted to a tuned RL- or a tuned RLC-shunt. Varying axial beam loads may change the beam's first mode resonance angular frequency ω_{sc} with short circuited (sc) transducer electrodes and the beam's first mode general coupling coefficient K_{33} of transducer P_3 in y-direction. Changes in both, ω_{sc} and K_{33} may influence the vibration attenuation with shunted transducers. To investigate the influence of varying loads F_x on ω_{sc} and K_{33}, the mathematical receptance model of the transducer P_3 is derived in frequency domain. The values of ω_{sc} and K_{33} for axial loads $F_x = [-1000, -500, 0, 500, 1000, 1500]\,\mathrm{N}$ are extracted from a least squares fit of the receptance model to the experimental data in frequency domain. As already shown by Kozlowski et al. [10], obtaining ω_{sc} and K_{33} from a curve fitting of the transducer receptance model results in a smaller error since the calculation of both parameters is less influenced by the used frequency resolution in the measurement.

1.3.1 Transducer Receptance Model

Figure 1.3 shows the electrical network representation of the piezoelectric transducer P_3 connected to the beam. The transducer P_3 is described by a gyrator-like two-port transducer network with its electrical capacitance C_p, a internal series resistance R_p and its transducer constant Y [12]. The vibration behavior of the beam's first mode with short circuited transducer electrodes is modelled by the modal mass m, the modal stiffness k and the assumed hysteretic damping with loss factor η resulting in the complex stiffness $k' = k\,(1 - i\,\eta)$.

The complex network receptance seen from the terminals 1 and 2 in Fig. 1.3 is obtained by

$$\alpha(\omega) = \frac{1}{i\,\omega\,Z(\omega)} \tag{1.1}$$

with excitation frequency ω. The impedance

$$Z(\omega) = \frac{U_3(\omega)}{I_3(\omega)} = \frac{Z_p(\omega)\,Z_1(\omega)}{Z_p(\omega) + Z_1(\omega)} \tag{1.2}$$

results from the parallel connection of the structural impedance $Z_1(\omega)$ of the first mode seen from the terminals 3 and 4 the transducer impedance

$$Z_p(\omega) = R_p - \frac{i}{\omega\,C_p}. \tag{1.3}$$

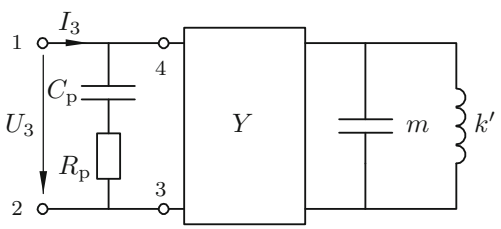

Fig. 1.3 Electrical network model of the piezoelectric transducers and the beam's first mode

The structural impedance of the first mode in y-direction

$$Z_1(\omega) = Y^2 \left(\frac{1}{Z_{\mathrm{m}}(\omega)} + \frac{1}{Z_{\mathrm{k}'}(\omega)} \right) = Y^2 \left(i\,\omega\,m + \frac{k\,(1+i\,\eta)}{i\,\omega} \right) \tag{1.4}$$

seen from the terminals 3 and 4 of the gyrator is the result of the parallel impedance of the modal mass $Z_{\mathrm{m}}(\omega) = \dfrac{1}{i\,\omega\,m}$ and the complex stiffness $Z_{\mathrm{k}'}(\omega) = \dfrac{i\,\omega}{k'}$. From (1.1) and (1.2), the receptance becomes

$$\alpha(\omega) = \frac{C_p}{\left(1 + \omega\,C_p\,R_{\mathrm{p}}\,i\right)} + \frac{1}{Y^2\,m\,\left(\omega_{\mathrm{sc}}^2 - \omega^2 + i\,\eta\,\omega_{\mathrm{sc}}^2\right)} \tag{1.5}$$

with the angular eigenfrequency $\omega_{\mathrm{sc}} = \sqrt{\dfrac{k}{m}}$. Furthermore, the term $\dfrac{1}{Y^2\,m}$ in (1.5) is replaced by $K_{33}\,C_{\mathrm{p}}\,\omega_{\mathrm{sc}}$, as suggested in [10], leading to the final expression of the transducer receptance

$$\alpha(\omega) = \frac{C_p}{\left(1 + \omega\,C_p\,R_{\mathrm{p}}\,i\right)} + K_{33}\,C_{\mathrm{p}}\,\frac{\omega_{\mathrm{sc}}}{\left(\omega_{\mathrm{sc}}^2 - \omega^2 + i\,\eta\,\omega_{\mathrm{sc}}^2\right)}. \tag{1.6}$$

1.3.2 Transducer Receptance Model Fit

In the model fit process, the parameters C_{p}, R_{p}, K_{33}, ω_{sc} and η in (1.6) are varied to solve the least squares curve fitting problem

$$\min_{C_{\mathrm{p}},\,R_{\mathrm{p}},\,K_{33},\,\omega_{\mathrm{sc}},\,\eta} ||\alpha(C_{\mathrm{p}},\,R_{\mathrm{p}},\,K_{33},\,\omega_{\mathrm{sc}},\,\eta,\,\omega) - \alpha_{\mathrm{exp}}(\omega)||_2^2 \tag{1.7}$$

where $\alpha_{\mathrm{exp}}(\omega)$ is the experimental data of the transducer receptance. Therefore, the *lsqnonlin* algorithm in MATLAB is used. Figure 1.4 shows the amplitude and phase response $|\alpha(\omega)|$ and $\arg\alpha(\omega)$ of the experimental data and the calculated receptance after the curve fitting for the axial load $F_x = 0\,\mathrm{N}$. Both, the model and the experimental data show a very good agreement.

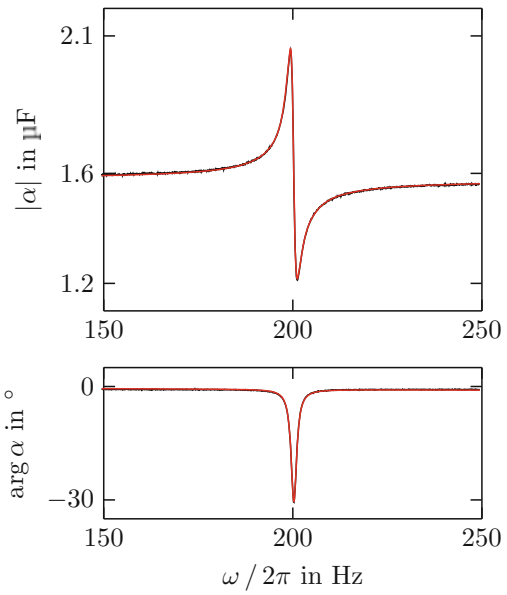

Fig. 1.4 Calculated transducer receptance (*red solid line*) with fitted parameters and experimental data (*black solid line*) for $F_x = 0\,\mathrm{N}$

1.3.3 Experimental Results of the First Eigenfrequency and Coupling Coefficient for Varying Axial Loads

As introduced before, a change of the resonance frequency ω_{sc} due to axial loads F_x will lead to a detuned vibration behavior of the RL- and RLC-shunt and, hence, the vibration attenuation capability will decrease. Apart from that, tensile and compressive axial loads may affect the electromechanical coupling coefficient K_{33} of transducer P_3. An increased coupling coefficient K_{33} will also increase the vibration attenuation capability with a RL-shunt, while a decreased K_{33} will also decrease the vibration attenuation potential. Furthermore, vibration stability issues with a RLC-shunt due to a changing coupling coefficient K_{33} are not investigated in this paper.

Figure 1.5a,b show the beam's first mode resonance frequency ω_{sc} and the beam's first mode coupling coefficient K_{33} of transducer P_3 extracted from the fitted receptance model (1.6) for axial tensile and compressive loads $F_x = [-1000, -500, 0, 500, 1000, 1500]$ N. In Fig. 1.5a, the resonance frequency ω_{sc} increases for an axial tensile load and decreases for an axial compressive load significantly. Compared to the axially unloaded beam with $F_x = 0$ N, the resonance frequency ω_{sc} increases by 6% and decreases by 10% for the extremes of the applied axial loads at $F_x = -1$ kN and $F_x = 1.5$ kN.

In contrast to the behavior of the frequency ω_{sc}, in Fig. 1.5b, the coupling coefficient K_{33} decreases for an axial tensile load and increases for an axial compressive load, as also shown by Lesieutre and Davis [13]. Compared to the axially unloaded beam with $F_x = 0$ N, the coupling coefficient K_{33} decreases by 6% and increases by 7% for the extremes of the applied axial loads at $F_x = -1$ kN and $F_x = 1.5$ kN.

Considering the absolute changes of the resonance frequency ω_{sc} and the coupling coefficient K_{33} in Fig. 1.5a,b axial tensile and compressive loads will decrease the vibration attenuation capability with the RL- and the RLC-shunt due to a detuning. For the RL-shunt with axial compressive loads, the increase in coupling coefficient and the associated theoretically increase of vibration attenuation capability will not be able to compensate the effects of a detuned ω_{sc} on the vibration attenuation capability, as it will be shown in the next section.

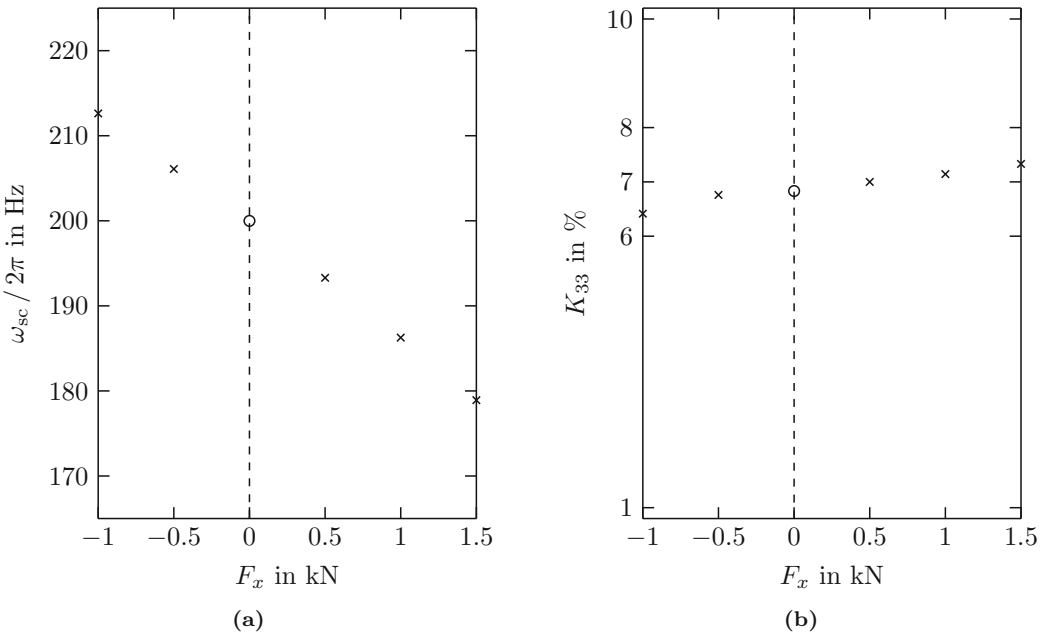

Fig. 1.5 Beam's first mode (**a**) resonance frequency ω_{sc} and (**b**) electromechanical coupling coefficient K_{33} of transducer P_3, for varying tensile and compressive axial loads F_x (*cross symbol*) and the axially unloaded beam $F_x = 0$ N (*open circle*)

1.4 Experimental Vibration Attenuation with RL- and RLC-Shunt for Varying Axial Loads

The vibration attenuation of the beam in case of the transducer P_3 is shunted to a RL-shunt and in case of P_3 is shunted to a RLC-shunt is compared for axial tensile and compressive loads $F_x = [-1000, -500, 0, 500, 1000]\,\mathrm{N}$, Fig. 1.6. As a measure for the vibration attenuation of the RL- and RLC-shunt, the frequency transfer function

$$H(\omega) = \frac{a(\omega)}{U_1(\omega)} \tag{1.8}$$

of the voltage excitation $U_1(\omega)$ of transducer P_1 to the beam vibration acceleration $a(\omega)$ is considered, Fig. 1.1. Additionally for the axially unloaded beam with $F_x = 0\,\mathrm{N}$, the vibration attenuation potential of the RL- and RLC-shunt is obtained from the comparison of $H(\omega)$ when the P_3 electrodes are short circuited and when shunted.

Figure 1.6a shows the amplitude and phase response $|H(\omega)|$ and $\arg H(\omega)$ when transducer P_3 is shunted to a RL-shunt with $R = 48.4\,\Omega$ and $L = 402\,\mathrm{mH}$. The values for R and L were tuned experimentally to give the highest reduction in amplitude in the considered frequency range. For the axially unloaded beam at $F_x = 0\,\mathrm{N}$, the vibration attenuation with RL-shunt is 15 dB. For varying axial tensile and compressive loads F_x, a significant decline in the vibration attenuation potential can be observed in the amplitude response. The decline in vibration attenuation is slightly higher for tensile loads. Furthermore, the detuning of ω_{sc} due to axial tensile and compressive loads is observed in the phase response by a shift of the 90° crossing frequency.

Figure 1.6a shows the amplitude and phase response $|H(\omega)|$ and $\arg H(\omega)$ when transducer P_3 is shunted to a RLC-shunt with $R = 4.8\,\Omega$, $L = 29.6\,\mathrm{mH}$ and $C = -1.69\,\mu\mathrm{F}$. The values for R, L and C were tuned experimentally to give the highest and stable reduction in amplitude in the considered frequency range. For the unloaded beam, the vibration attenuation with RCL-shunt is 26 dB and, as expected, is significantly higher than with the RL-shunt. For varying axial tensile and compressive loads F_x, the observed decline in the vibration attenuation capability is smaller compared to the RL-shunt. The decline in vibration attenuation, again, is slightly higher for tensile loads.

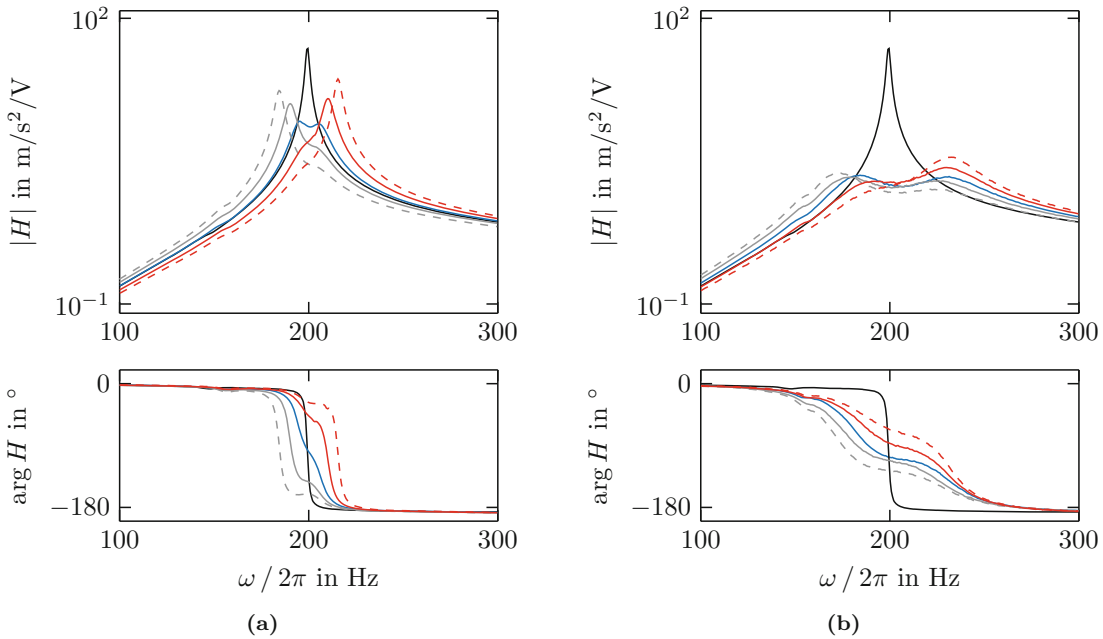

Fig. 1.6 Amplitude and phase response of $H(\omega)$, short circuited (*black solid line*), with (**a**) RL-shunt and (**b**) RLC-shunt, for the unloaded beam (*blue solid line*) with $F_x = 0\,\mathrm{N}$ and varying axial loads F_x : $+500\,\mathrm{N}$ (*gray solid line*), $+1000\,\mathrm{N}$ (*gray dashed line*), $-500\,\mathrm{N}$ (*red solid line*), $-1000\,\mathrm{N}$ (*red dashed line*)

To conclude, vibration attenuation with a RLC-shunt is less sensitive to varying axial tensile and compressive loads. However, using a negative capacitance may lead to stability issues, but they were not observed in the performed experiments and are not part of this paper.

1.5 Conclusion

Vibration attenuation of a beam with a circular cross-section by piezo-elastic supports with one transducer shunted to RL- or RLC-shunt subject to varying axial tensile and compressive loads is experimentally investigated. When no shunt is connected to the transducer, the first beam's mode resonance frequency significantly increases and decrease in consequence of axial tensile and compressive loads. Compared to the unloaded beam, the relative changes of the electromechanical coupling coefficient are in the same order of magnitude as for the resonance frequency, but, the absolute change of the coupling coefficient has no significant effect an the vibration attenuation with RL- and RLC-shunt. The resonance frequency detuning due to axial tensile and compressive loads results in a declined vibration attenuation when shunting the transducer to a RL- or a RLC-shunt. As observed in the measured frequency transfer functions, the RLC-shunt is less sensitive to uncertain axial loads then the RL-shunt.

Acknowledgements The authors like to thank the German Research Foundation DFG for funding this research within the SFB 805.

References

1. Hagood, N.W., von Flotow, A.H.: Damping of structural vibrations with piezoelectric materials and passive electrical networks. J. Sound Vib. **146**(2), 243–268 (1991)
2. Moheimani, S.O.R., Fleming, A.J.: Piezoelectric Transducers for Vibration Control and Damping. Springer, London (2006)
3. Beck, B.S.: Negative capacitance shunting of piezoelectric patches for vibration control of continuous systems. PhD thesis, Georgia Institute of Technology (2012)
4. Niederberger, D.: Smart damping materials using shunt control. PhD thesis, Swiss Federal Institute of Technology Zürich (2005)
5. Neubauer, M., Oleskiewicz, R., Popp, K., Krzyzynski, T.: Optimization of damping and absorbing performance of shunted piezo elements utilizing negative capacitance. J. Sound Vib. **298**, 84–107 (2006)
6. Hagood, N.W., Crawley, E.F.: Experimental investigation of passive enhancement of damping for space structures. J. Guid. Control. Dyn. **14**(6), 1100–1109 (1991)
7. Hagood, N.W., Aldrich, J.B., von Flotow, A.H.: Design of passive piezoelectric damping for space structures. NASA Contractor Report 4625 (1994)
8. Preumont, A., de Marneffe, B., Deraemaeker, A., Bossens, F.: The damping of a truss structure with a piezoelectric transducer. Comput. Struct. **86**, 227–239 (2008)
9. Götz, B., Schaeffner, M., Platz, R., Melz, T.: Lateral vibration attenuation of a beam with circular cross-section by a support with integrated piezoelectric transducers shunted to negative capacitances. Smart Mater. Struct. **25**(095045), 10 (2016)
10. Kozlowski, M.A., Cole, D.G., Clark, R.L.: A comprehensive study of the RL series resonant shunted piezoelectric: a feedback controls perspective. J. Vib. Acoust. **133**, 011012-1–011012-10 (2011)
11. Enss, G.C., Gehb, C.M., Götz, B., Melz, T., Ondoua, S., Platz, R., Schäffner, M.: Device for bearing design elements in lightweight structures (Festkörperlager) (2016)
12. Lenk, A., Ballas, R.G., Werthschützky, R., Pfeifer, G.: Electromechanical Systems in Microtechnology and Mechatronics. Number 978-3-540-89320-2. Springer, Berlin (2011)
13. Lesieutre, G.A., Davis, C.L.: Can a coupling coefficient of a piezoelectric device be higher than those of its active material? J. Intell. Mater. Syst. Struct. **8**, 859–867 (1997)

Chapter 2
Correlation of Non-contact Full-Field Dynamic Strain Measurements with Finite Element Predictions

Ibrahim A. Sever, Martyn Maguire, and Jose V. Garcia

Abstract It is highly desirable to have the capability to measure strain maps on components directly and in a full-field fashion that addresses shortcomings of conventional approaches. In this paper, use of a 3D laser measurement system is explored for direct and full-field dynamic strain measurements on compressor and turbine rotor blades. More importantly, the results obtained are numerically correlated to corresponding FE predictions in a systematic manner. The ability to measure strain maps on real engine hardware is demonstrated not only for low frequency fundamental modes, but also for challenging high frequency modes. Correlation results show a high degree of agreement between measured and predicted strains, demonstrating the maturity of the technology and the validity of the method of integration used here. The measurements are repeated for a number of different loading amplitudes to assess the variations in strain fields. Although the application of 3D laser systems to measurements of full-field strain were explored in previous studies, to the best knowledge of authors, full-field numerical correlation of full-field strain on a wide range of real, complex components to this extent is presented here for the first time.

Keywords Model validation • Full-field strain • 3D SLDV • Correlation • Non-contact

2.1 Introduction

The ability to measure dynamic strain on components subjected to high vibratory stresses is very important as these measurements then directly feed into all important endurance/life calculations. Historically this requirement has been fulfilled in two main ways. The first and most widely used approach is the application of strain gauges. Although a direct measurement and still a very popular practice; there are a number of shortcomings. Firstly, they are intrusive as they have to be bonded to the component. Typically only a few of these can be used which do not provide a representative spatial coverage nor are they enough to evaluate changing strain patterns due to load variations. Their nontrivial footprint means that they can only provide average strain under the area they cover. The second approach, albeit less common, is to validate a finite element model of a given component through direct measurements of displacement, velocity or acceleration and then to use that improved model for predictions of strain and stresses. Although effectively used, particularly in case of full-field measurement systems such as Scanning Laser Doppler Vibrometers (SLDV), good level of correlation with these measurements does not always translate to a good correlation in strain. Moreover, when it comes to components showing complex phenomena or those made from novel materials, the confidence in original FE models is often low or such FE models may not even exist; rendering strain predictions obtained this way even less reliable.

Non-contact and full-field measurements of 3D vibration responses have been explored via a number of different technologies over the years. Earlier systems using double-pulse Electronic Speckle Pattern Interferometry (ESPI) exploited different combinations of viewing and observation directions [1, 2] vibration measurements. Systems with 3-observation and 1-illumination directions as well as 3-illumination and 1-observation directions were explored however recovery of full-field dynamic strain for industrial applications and high frequency complex mode shapes were not reported. A creative way in

I.A. Sever (✉)
Rolls-Royce Plc, SinA-33, PO Box 31, Derby, DE24 8BJ, UK
e-mail: ibrahim.sever@rolls-royce.com

M. Maguire
Rolls-Royce MTOC, Kiefernstraβe 1, D-15827 Blankenfelde-Mahlow, Germany

J.V. Garcia
GP4-4, PO Box 3, Bristol, BS34 7QE

R. Barthorpe et al. (eds.), *Model Validation and Uncertainty Quantification, Volume 3*,
Conference Proceedings of the Society for Experimental Mechanics Series, DOI 10.1007/978-3-319-54858-6_2

which a 1-D SLDV system is used in combination with a short-focus lens to recover 3D vibration information was given in [3] however obtaining full-field coverage this way is simply not practical. A detailed review of Digital Image Correlation (DIC) techniques applied to vibration measurements explored suitability of DIC technology compared with more conventional methods and SLDV based systems [4], however, similar to double pulse ESPI, the use of DIC based systems outside quasi static regime and for high frequency complex modes has been limited. Recently 3D SLDV based measurement systems have gained popularity due to their practicality for complete dynamic deformation field (i.e. 3D) measurements. A through study of strain measurements with a 3D SLDV system is given in [5]. Although comparison with FE and conventional strain gauge results are presented, these are done at the locations of strain gauges only, rather than in full-field sense, such as in the form of strain MAC and strain CoMAC.

The pursuit of more direct, high density and high accuracy measurements in this study is motivated in particular by their potential to provide better model validation opportunities. Valid models (i.e. models that are demonstrated to be adequate representation of real life behaviour) provide unique opportunities as they can enable simulation of behaviour for a wide range of parameter ranges and constraints that may not be practicable or cost effective to do through testing. Given the criticality of the use of these models, such as in estimating the stress and strain fields and ultimately the structural integrity of aero-engine components, ensuring that they are valid to an acceptable degree is essential. This is something that has been mainly done via measurements of displacement mode shapes as these are the easiest to measure. The inferred conclusion from such measurements is that when the displacement shapes are shown to match with a sufficient degree of correlation, the resulting stress and strain distributions will follow the same trend. However the more direct and the more detailed the measurements of parameters of interest are, such as strain and stress distributions, the higher will be the confidence one can have in simulation models these data are used to asses and, if necessary, to correct.

2.2 Measurement Campaign

Measurements of full-field strain on aero-engine blades using a 3D SLDV system were reported in an earlier publication [6]. Although in this paper the focus is on the correlation of results, particularly those of full-field strain, with the FE model predictions, it is worthwhile reviewing the basic principles of measurement system as well as hardware tested and the setup used.

2.2.1 Measurement System

A 3D Scanning LDV system is used in acquisition of displacement and strain measurements. A picture of the measurement system in use is given in Fig. 2.1a. The principle behind the operation of an LDV transducer can be explained simply as follows [7]: light produced by a laser source is split into two beams of the same amplitude by a beam splitter, one directed to a fixed reference and the other to the vibrating target. Following the same path back, the beams are combined by the same splitter and send to a photodetector. Since the light from the target is optically mixed with an equally coherent reference beam and heterodyned on the photodetector surface, the resolution of the sign of the vibration velocity is achieved by pre-shifting the reference beam's frequency by a known amount. The signal received by the photodetector is then frequency demodulated by a suitable Doppler processor and the vibration velocity of the target is worked out. The 3D SLDV system used during this measurement campaign was a PSV 500 3D. All simple out-of-plane 1D measurements were made using a Polytec PSV 400 HS. The 3D system consists of three independent SLDV heads as shown in Fig. 2.1a. Fundamental mode of operation for 1D and the 3D systems are identical in that each laser transducer captures the vibration response on the structure along its own line of sight. The fact that there are three such observation directions in the 3D case is being exploited to recover the complete vibration response in three orthogonal directions. This requires that all three SLDVs are coordinated and that the measurement surface is precisely aligned to a degree where laser beams from all SLDVs are coincident to within an acceptable tolerance. Alignment requirements are stricter for strain estimations than they are for the displacement measurements.

Fig. 2.1 (**a**) 3D SLDV measurement system in use, and (**b**) Intermediate pressure compressor blade (*left*) and intermediate pressure turbine blade (*right*)

2.2.2 Test Hardware

The measurement campaign is carried out on a number of aero-engine components including intermediate pressure compressor and turbine blades and a full-size fan blade (not shown here). Some of these components are shown in Fig. 2.1b. In case of compressor and turbine blades, tests are repeated for a number of different excitation levels. These components feature a number of different challenges in terms of clamping conditions, frequency range they cover and the complexity of modes of vibration they poses. As such they should provide appropriate coverage for demonstration of the capability being presented. Strain as well as displacement measurements are carried out for all components however in this paper the correlation of strain measurements is carried out for the compressor blade alone.

2.2.3 Test Environment and Setup

In order to eliminate the adverse effects that the environment might have on the measurements, the testing was carried out in a state-of-the-art vibration test facility. Vibration isolation is achieved through the use of large air-sprung bed plates, and the temperature is maintained at a suitable level. Thick, well insulated test cell walls ensure that there is no interference from external sources. The measurement process was largely automated which meant that once alignment was achieved no user intervention was required. As alignment was based on the engine coordinate system it was repeatable.

Components tested here were fixed at their roots with appropriate clamping mechanisms, mimicking similar boundary conditions to those present in engine. Various excitation techniques were used depending on the size of the component. Turbine blades were excited via an acoustic horn pressure unit and a bespoke piezoelectric resonator. Most tests on these components were performed using the pressure unit as it proved more effective. For larger components (i.e. compressor and fan blades) acoustic speakers were found to be more appropriate where suitable speakers were selected proportional to size of the components being excited.

Measurement grids on blade surfaces to be scanned were carefully optimised in a separate test planning process to maximise observability of the modes on interest (e.g. maximise ability to distinguish them without any ambiguity) using nominal FE models present. This ensured that the measurement grid was defined in the engine coordinate system. This is a major advantage as this grid is then transferred to the measurement system and measurement volume is calibrated in a way that corresponds to the FE environment, making the alignment and correlation of FE and test points much easier. Much denser grids were used in strain measurements, compared with the ones used in displacement mode shapes. Also a much more accurate laser alignment process had to be used in strain measurement case which in return made the strain measurements a longer campaign.

2.3 FE Model and Test Planning

Test planning for the measurement campaign was carried out using the nominal FE models for the blades tested. Provided that there are no fundamentally significant deviations, this is acceptable as the character of modes and the frequency ranges derived from the nominal models provide appropriate guidelines for defining the overall boundaries of the test campaign. However, it is well known that due to manufacturing tolerances, the physical parts show variations from their design intent. As these tolerances are often defined by manufacturability and performance constraints, their impact on structural dynamics may be non-trivial. The impact of these variations on the overall correlation study will be explored in future publications. For the sake of introducing the correlation methodology, all FE models used in this study will be those derived from the nominal geometry but with appropriate boundary conditions to reflect the test configuration.

Planning of the test campaign consists of defining the measurement grid and assessing the suitability of this grid in capturing vibration modes of interest. FE model of the compressor blade, measurement grids for displacement and strain mode shapes, and, auto correlation matrix of the displacement modes captured by identified measurement grid are all given in Fig. 2.2a, b and c, respectively.

In the case of displacement mode shapes, the effective independence method [8] is used for down selection of measurement points. Given that an optical measurement system is used, the candidate nodes to choose from are the ones that lie on the surface that can be measured (see Fig. 2.2a), rather the whole FE model. Suitability of this grid is confirmed by Auto Modal Assurance Criterion (autoMAC) plot given in Fig. 2.2c. Here the predicted modes of the nominal FE model

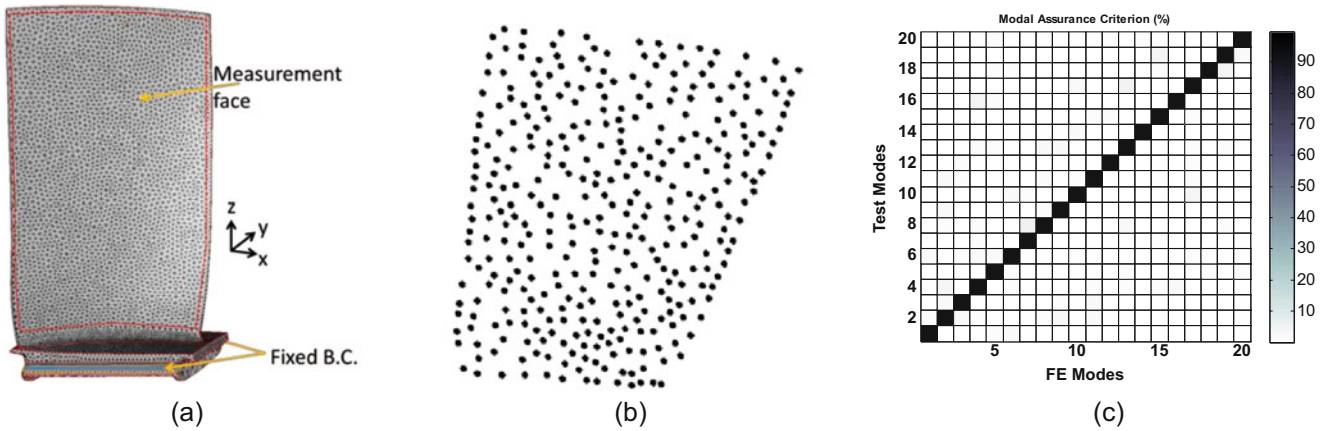

Fig. 2.2 (**a**) Compressor blade FE model, (**b**) Measurement grid used displacement mode shapes, (**c**) resulting auto-MAC plot

sampled at measurement nodes are compared to themselves. Cross-mode correlation amplitudes as evident from trivial off-diagonal terms (all below 10%) suggest that all measured modes should be uniquely identifiable.

Measurement grid for the strain mode shapes is significantly denser than the one for displacement mode shapes. This is required to capture the local strain variations faithfully. Note that by this stage the modes are already identified through correlation of displacement mode shapes. As such autoMAC check performed for displacements is not necessary to repeat for strain.

2.4 Correlation of Mode Shapes

Measurement grid given above was identified for the displacement mode shapes using the full deformation field. In other words all X, Y and Z displacement DOFs were used at each measurement grid as the same DOFs would be captured from the tests. Measurement of all DOFs at each point is a requirement for strain measurements but it is not essential for displacement mode shapes. In fact 1-D SLDVs, measuring a projection of total deformation field in the line of sight, have been used for decades. Nevertheless, availability of all DOFs brings significant advantages in the form of increased independent information which even in the case of displacement mode shapes can make a big difference.

Figure 2.3 shows a particular mode measured on the intermediate pressure turbine blade by 1-D and 3-D SLDV systems, together with the predicted FE mode shape where FE and the 3-D measured mode shape are almost identical. Although the 1-D measurement appears to be very different, a direct comparison is inappropriate. 1-D SLDV measures a projection of overall response in the viewing direction whereas distributions shown for the FE and the 3-D SLDV are for the resultant displacements from all DOFs computed and measured. A correct correlation in the case of 1-D SLDV measurements would be with FE predictions projected in a similar way to reflect the operation of 1-D SLDV system.

Having said that, the fact remains that the 3-D SLDV provides a lot more information (three times as much) about the deformation field, which in return allows better identification of measured mode shapes. This is demonstrated in Fig. 2.4. Here there are two correlation scenarios shown where mode shapes captured by 1-D and 3-D SLDV systems are correlated in the form of Modal Assurance Criterion (MAC) with their corresponding FE predictions in Fig. 2.4a and b, respectively. Significant off-diagonal values in 1-D SLDV case which lead to difficulties in identifying mode shapes unambiguously are greatly reduced in the 3-D case where the identification of the modes is now straight forward.

Displacement mode shape measurement campaign performed on the compressor blade is summarised in Fig. 2.5. As evident from the sub-set of measured and predicted mode shapes given in Fig. 2.5a, not only the global behaviour but also the local variations are extremely closely matched. MAC matrix given in Fig. 2.5b shows a remarkable degree of correlation between measurements and the predictions with MAC values at 95% and above, and, with all off-diagonal values below 10%. It is worth noting the extraordinary similarity between autoMAC plot generated in Fig. 2.2c and the MAC plot given in Fig. 2.5b. As such the FE model is demonstrated to be a good representation of the measurement hardware from mode shapes point of view.

This level of accuracy in the resultant correlation also demonstrates that tests are carried out as planned and that the alignment of FE model and the test model is performed adequately. The latter is a critical factor, particularly for mode shapes

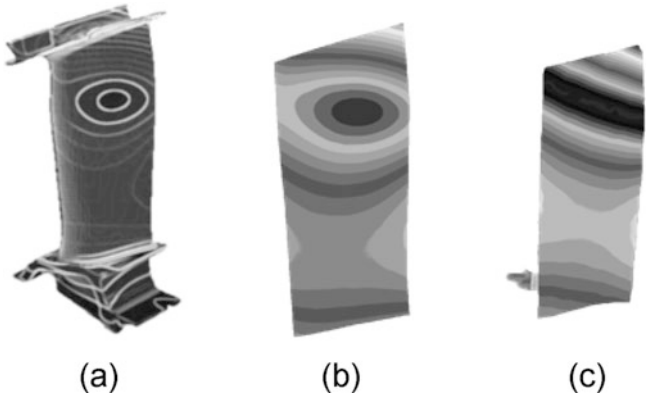

Fig. 2.3 (**a**) Predicted FE mode shape, (**b**) 3-D SLDV measurement, and (**c**) 1-D SLDV measurement

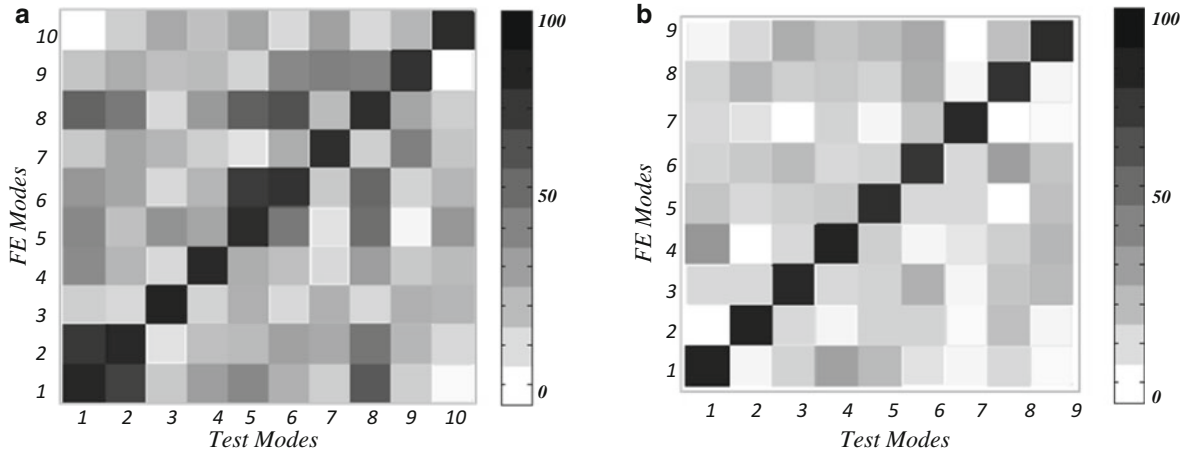

Fig. 2.4 Mode shape correlation (%) for the turbine blade using (**a**) 1-D SLDV, and (**b**) 3-D SLDV measurements

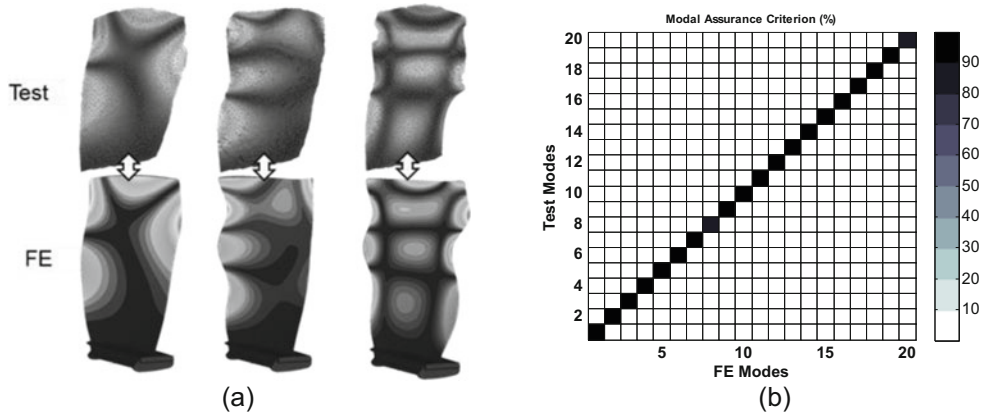

Fig. 2.5 (**a**) Sub-set of measured and predicted compressor blade mode shapes, (**b**) MAC matrix of displacement mode shapes

with complicated, localised variations and therefore needs appropriate care. One important point to note in the case full-field measurements of this kind is that, unlike conventional accelerometer or strain gauge etc. measurements where test grid is much less refined, the measurement grid can be denser than the corresponding distribution of the FE nodes. This is often not an issue for displacement mode shape measurements where the measurement grid is optimised using the FE model and therefore guaranteeing the alignment measurement points with the FE nodes. However the same is not necessarily the case for strain measurements where the density of test points can be much higher or when the model used in test planning and correlation are different (e.g. reversed engineered FE models).

2.5 Correlation of Full-Field Strain Measurements

Following the measurements of mode shapes on the turbine and compressor blades, a number of modes were identified for the measurement of full-field strains. Up to 12 modes covering the low, middle and high frequency range of modes identified in mode shape campaign were targeted. This enabled suitable coverage of complexity in terms of shapes targeted as well as allowing manageable measurement times. One important difference between displacement mode shape and strain mode shape measurements was the measurement grid used. Figure 2.6a shows the grid used for displacement measurements whilst Fig. 2.6b shows that used for strain. There are six times as many points in the strain grid as there are in the displacement grid. Since this density is much finer than the density of the FE nodes on the target surface, the new grid had to be created in the measurement system. The care was taken to ensure an overall regular distribution of points; however, the density was markedly increased around the edges and at areas where high gradient variations were expected.

Strictly speaking, mostly strain operational deflection shapes (ODSs) rather than true strain mode shapes are measured. Due to base and acoustic excitation techniques used in the tests, measuring the actual force driving the components was not possible. However, in case of strain measurements to be used in quantified correlation with FE predictions, the input voltage into generator was used as a reference signal.

The theory behind estimation of surface strain distributions from displacement measurements can be found in various publications [5, 9]. A triangular mesh is generated for the strain grid and virtual strain gauges are placed at each edge of each triangle as shown in Fig. 2.6c. For the grid shown in (b) this corresponds to having a total of 1800 virtual strain gauges. As described in [10], the displacements are transformed to the plane of surface triangles in the form of 2 in-plane and one out-of-plane components. Using these components strains are calculated for all surface triangles before being transformed back into global coordinate system.

Another critical difference between displacement and strain measurements is that the alignment precision required for strain measurements is much higher. The first step in measurements with the 3-D SLDV, regardless of whether displacement or strain is measured, is to perform the 3-D alignment. When the main vibration response is out-of-plane, such as is the case for turbine and compressor blades used in this work, potential crosstalk between out-of plane and in-plane components results in large errors, particularly for weak in-plane components. This is especially a challenge for strain calculations which relies on accurate resolution of weak in-plane, as well as strong out-of-plane displacements. To avoid these errors, alignment of all three laser beams with respect to measurement point should be ensured, i.e. all three beams should intersect on the measurement point. This, in Polytec 3-D SLDV system used in this study, is achieved via a process called video triangulation. More information on video triangulation can be found in [11] where the basic idea is the identification of the positions of the three beams in the video image by image processing. Once this is done, corrections to the mirror angles are applied until the beams meet precisely at the measurement point. To guarantee the best results, the video triangulation is performed at each such point. Since the alignment is done prior to measurements at each point, beam drift problems are eliminated, resulting in reliable and consistent alignment throughout the measurement session. Although performing video triangulation at each point results in considerably long measurement times, for a given setup, this needs to be done only once. Subsequent measurements can be performed much faster as the alignment information for each point is reused.

A sweep sine test was performed before strain measurements and this was repeated each time a configuration changed or ambient conditions were different to make sure that the exact natural frequencies at the time could be identified. Then the

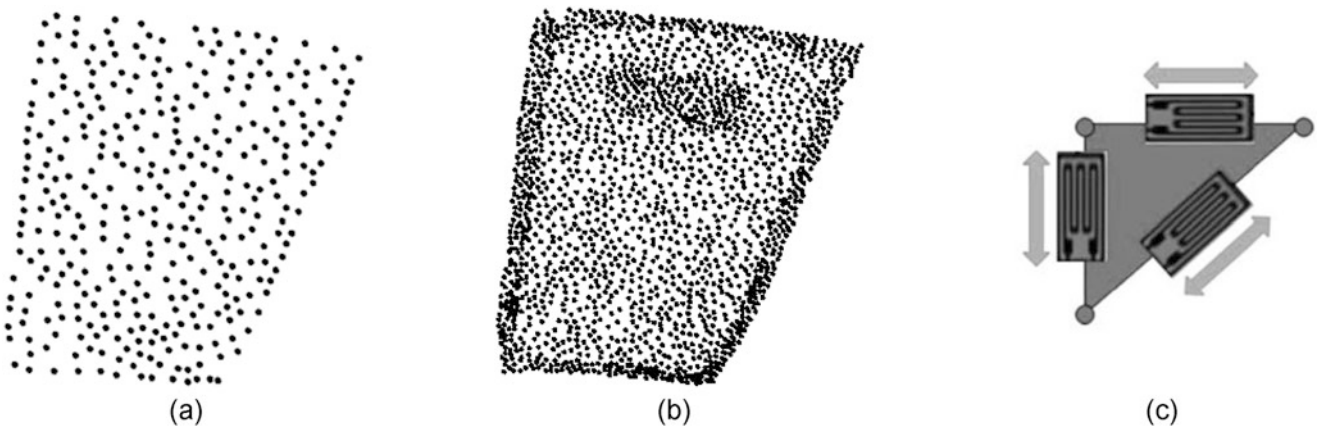

Fig. 2.6 (**a**) Displacement measurement grid, (**b**) strain measurement grid, and (**c**) placement of virtual strain gauges (taken from [10])

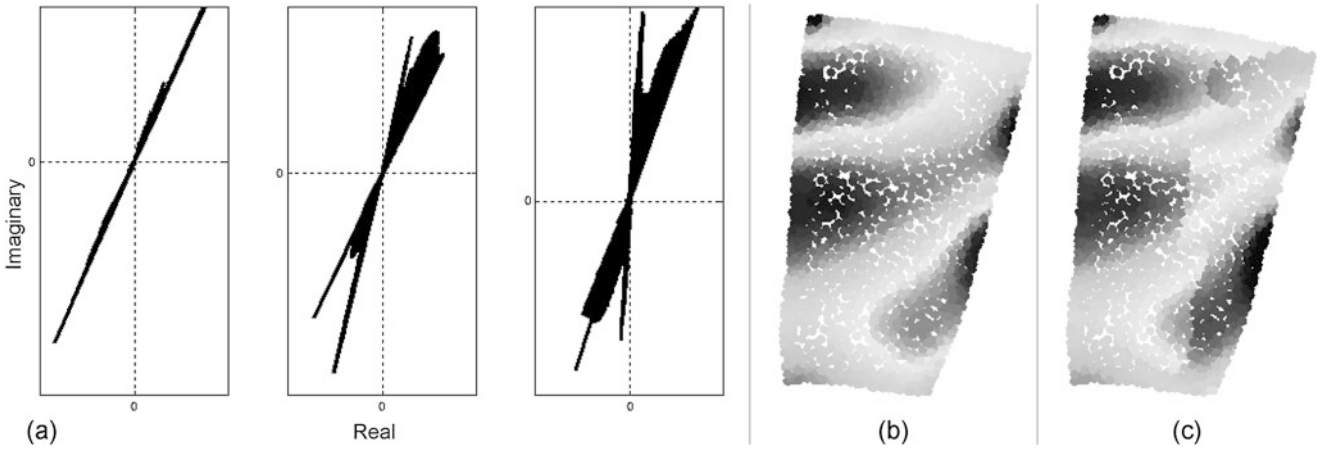

Fig. 2.7 (**a**) Strains on complex plane. Correct (**b**), and, incorrect (**c**) realisation of surface strain

strain measurements were performed in two ways. First, a number of selected modes were excited all at once by generating a multi-sine signal composed of natural frequencies of these modes. Since in this case the input energy was shared across all available components, each mode could only be excited to low amplitudes. In the second way, tests were repeated by concentrating on each mode separately. Since only one frequency was output at any given time, higher response amplitudes could be achieved. Performing measurements at different amplitudes this way was targeted as it would allow assessment of any potential dependency of strain distributions to response amplitudes. In this context multi-sine testing provided a time-efficient way of acquiring low-amplitude strain distributions for modes of interest.

Strain mode shapes estimated from the 3-D SLDV system are complex in mathematical sense and are often output in terms of real and imaginary parts. To be able to compare and correlate with FE predictions which are real-valued (e.g. signed amplitudes), a further processing of measured strains is needed to "realise" these otherwise complex quantities. Figure 2.7a shows Argand diagram representation of a number of strain mode shapes measured on the compressor blade together with results of some realisation attempts in Fig. 2.7b and c. It is evident from the co-linearity of the complex vectors that the underlying strain mode shapes are mainly real, albeit rotated in the complex plane. These vectors need to be appropriately "realised" by rotating them to align with x-axis and by removing remaining small complexities.

Care should be taken whilst performing the realisation to ensure unrealistic phase boundaries are not created, as illustrated in Fig. 2.7c, which in turn impact quantified correlation between measurements and the predictions. It is possible to do the realisation manually however it prolongs the process and does not allow batch processing in an automation environment. To this end, an algorithm is developed via which it is possible to identify the best-fit rotation of the vectors automatically for realisation of estimated surface strains.

Figure 2.8 shows strain measurement results on the compressor and the turbine blades for a number of modes as well as the predicted strain distributions from their nominal FE models. All six components of surface strain are estimated however only strains in z-direction are shown in the plots and used in the subsequent correlation processes.

Since the contouring used in the FE package in construction of predicted strain mode shapes is independent of the one used in the measurements, both sets of shapes may appear different at first sight. However, at a closer inspection the predicted and measured strain mode shapes given in Fig. 2.8 show a remarkable degree of similarity. This is true for high frequency complex modes (right hand side) as well as for low frequency fundamental modes (left hand side) where the evident similarity may more readily be expected.

Although visual examinations are often the first port of call, a more fundamental insight can only be obtained by performing a proper quantified correlation. To this end well documented displacement mode shape correlation metrics were used. Overall similarity of measured strain mode shapes with corresponding predictions was performed via MAC, and, the role of individual DOFs in this similarity, or lack of, was quantified via CoMAC. Utilising the same definition given for displacement mode shapes in [12]; MAC between measured, S_A, and a predicted, S_X, strain mode shapes is calculated as $MAC(A,X) = (|\{S_X\}^T\{S_A\}|^2)/(\{S_X\}^T\{S_X\})(\{S_A\}^T\{S_A\})$. This is a value between 0 and 1, with 1 representing identical mode shapes. However, in the plots and tables given here it is converted to percentages. Plot given in Fig. 2.9b shows the familiar MAC matrix, this time computed for the strain mode shapes. As mentioned before this is not strictly necessary as by this stage the mode pairing should already have been established through displacement mode shape MAC. Nevertheless it is given here to show that the mode pairing could equally be done using the strain MAC.

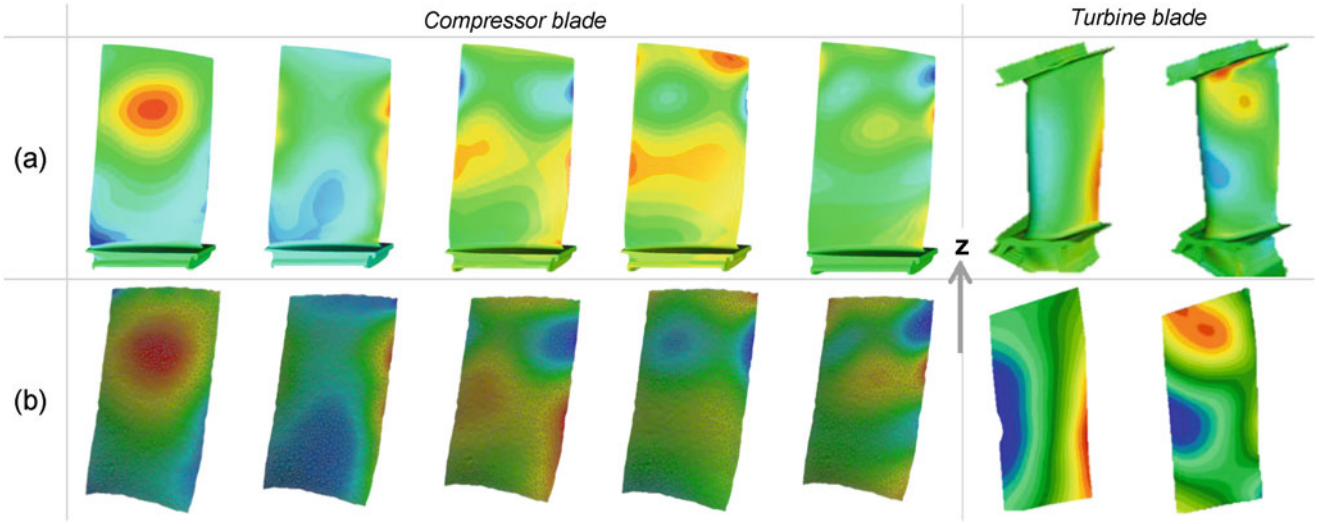

Fig. 2.8 (**a**) Predicted strain, (**b**) measured strain. *[both in z-direction]*

Pair #	ω_n diff (%)	MAC (%)
1	-1.3	89
2	-2.2	96
3	2.3	91
4	-0.1	97
5	3.2	84
6	-1.7	89
7	2.8	91
8	1.4	68
9	-1.2	73
10	-1.4	79
11	-1.5	71
12	-2.2	80

(a)

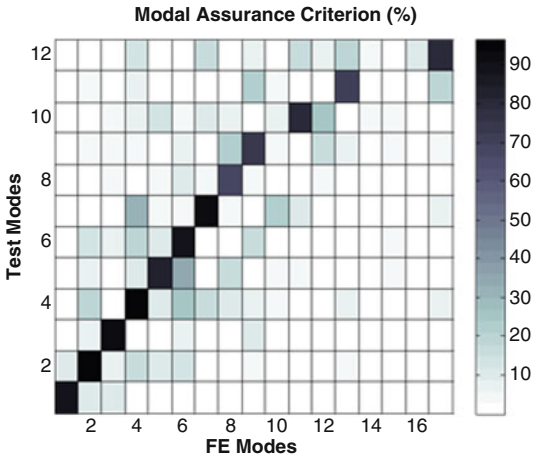

(b)

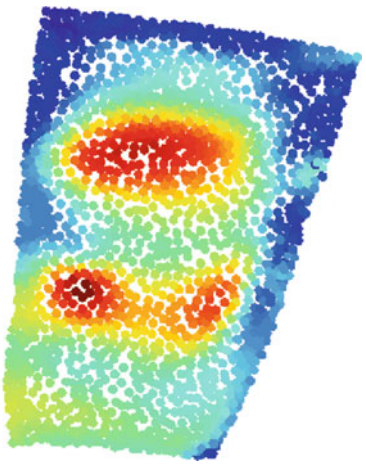

(c)

Fig. 2.9 (**a**) Quantified correlation of paired strain mode shapes and natural frequencies, (**b**) strain MAC matrix, and, (**c**) strain CoMAC (z-direction, *blue*➔low CoMAC, *red*➔high CoMAC)

Although the MAC is a very useful parameter, it is also a global similarity metric and does not necessarily give any insight into distribution of correlations across DOFs used. Coordinate MAC or CoMAC has been developed for this purpose [12], and for an individual DOF, i, it can be calculated across all correlated mode pairs as $CoMAC(i) = \left(\sum_{n=1}^{N} |(S_X)_{in}(S_A)_{in}|^2\right) \Big/ \left(\sum_{n=1}^{N} (S_X)_{in}^2 \cdot \sum_{n=1}^{N} (S_A)_{in}^2\right)$. This is a value between 0 and 1. Here N represents total number of paired modes. The list of paired modes used in strain CoMAC calculations for the compressor blade is given in Fig. 2.9a. Low values of CoMAC indicate DOFs that have relatively low contributions to overall correlation. Although locations of these DOFs are where the differences between the test and the mathematical model manifest themselves, they are not necessarily the locations responsible for the said differences.

Having warned against temptation to brand low CoMAC areas as the sources of discrepancies, the fact remains that the plot given in Fig. 2.9c presents a very regular distribution. Even if this cannot readily be identified form the plot, it is perfectly reasonable to presume a systematic discrepancy being present and this can be a very useful tool in identification of potential sources of such discrepancies between the FE model and the test. It is not hard to see that once such connections between CoMAC variations and underlying causes are established, effectiveness of model updating efforts can be significantly improved.

A CoMAC plot of this kind, to the best of authors' knowledge, is presented here for the first time. Therefore there is very little experience with what it might potentially reveal. However given that it is the result of direct strain measurements, it may point to potential discrepancies between simulation and test more directly. Nevertheless this is at best a speculation at this stage and requires a systematic study to establish with clear evidence.

Overall, the results given in Fig. 2.9 constitute a remarkable body of evidence for success of full-field non-contact strain measurements and more importantly for quantified correlation with their predicted counterparts. Up to 12 mode pairs, spanning the full operational range of the selected engine component, are identified with average MAC value of 84% with most of the modes near 90% or higher.

Nevertheless, some of the mode pairs have markedly low MAC values. There are a number of potential reasons for this. First of all, the measured results are compared with the nominal FE model constructed from the design intent. The test hardware has inevitable deviations from this design intent due to manufacturing tolerances. Furthermore, the blade model is simulated with fixed boundary conditions applied to its root whereas the actual fixture has a finite flexibility with potential nonlinear interactions due to contact and friction. Both of these causes need further exploration and they will be addresses in future studies.

One additional source for discrepancies has to do with the alignment errors during the process of matching measurement points with the FE nodes or in short; node-point pairing. In cases where the test planning for identification of measurement points is performed on the FE model that is used in eventual correlation, this errors should be very low. However as explained above, even when this is done model and real hardware geometries will not exactly match and there will be deviations. In the present case the test planning was carried out for the displacement mode shape measurements. As this grid was not dense enough for strain measurements, it was made denser in the measurement environment by manually adding new data points. As these new points could not be guaranteed to coincide with FE nodes, they were paired with the nearest ones which resulted in inevitable discrepancies. Node-point pairing done for strain correlation of the compressor blade is given in Fig. 2.10. Magnified portion given therein demonstrates the point being made here where measurement points are often outside circles representing FE node targets.

Although alignment errors can be reduced by generating the strain grids from the FE model, eliminating them completely is not viable. Inevitably, differences between simulated and real geometries will exist. Moreover, sometimes FE nodes present on the surface to be measured may not be dense enough for strain measurements whereby new points will have to be manually added. A better solution to this issue would be to map the measurement grid to the simulation surface as accurately as possible and then interpolate FE predictions at the actual measurement points. This will greatly reduce the alignment errors. Given that the density of the measurement points is often sufficiently high compared with the surface strain variations, the interpolations could be done linearly without having to resort to more sophisticated methods.

It is often assumed that the strain values scale up with vibration amplitudes linearly, preserving the shape of distribution. Although linearity checks are factored into any serious test campaign wherever this is assumed, it is not always straightforward to capture it with conventional strain measurement means such as with strain gauges. Amplitude dependent variations could be quite complex and distributed which render discrete measurements unsuited to the task. Full-field strain measurements provide a unique insight into capturing such variations, if present.

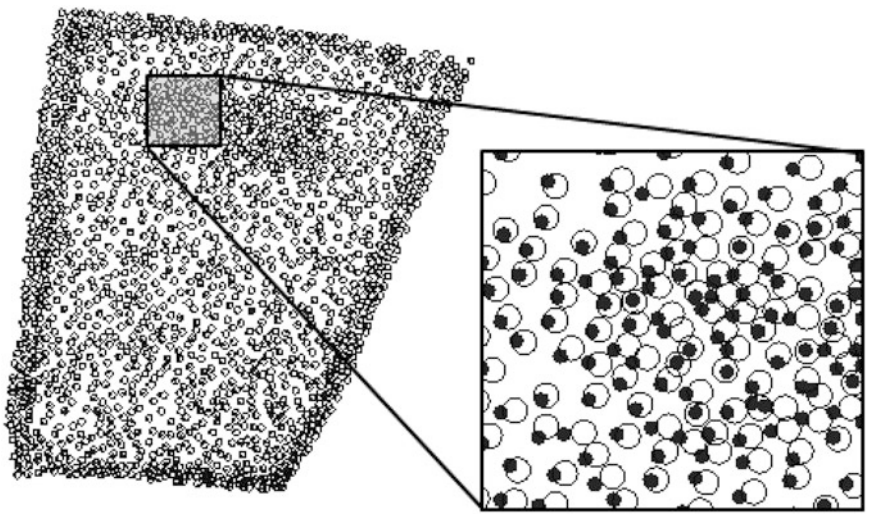

Fig. 2.10 Node-point alignment errors

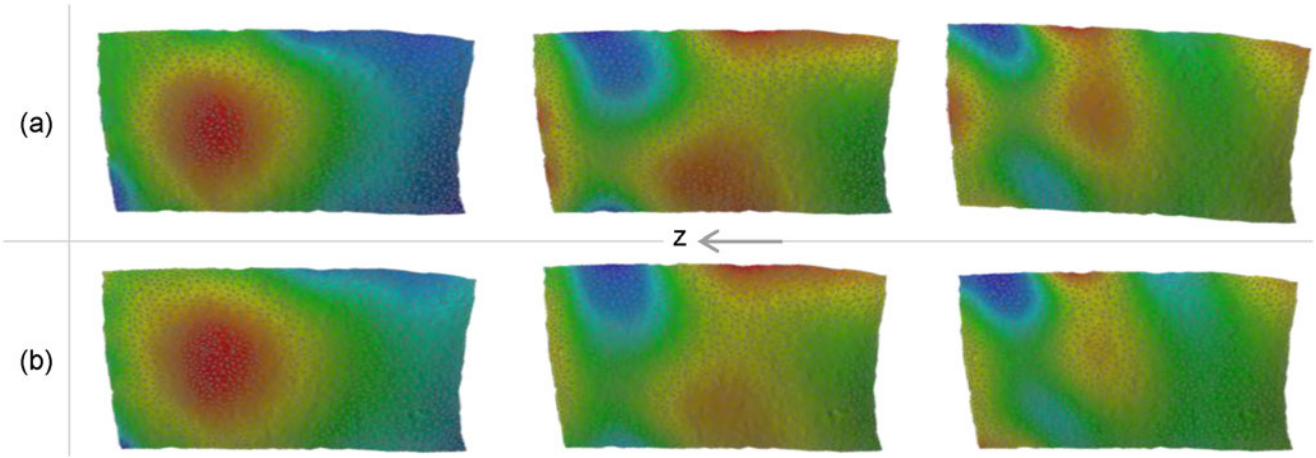

Fig. 2.11 (**a**) High-excitation, (**b**) low-excitation. [both in z-direction]

As explained earlier, the strain measurements were repeated at low and relatively high vibration amplitudes for this purpose. The resultant strain shapes for a number of selected compressor blade modes are given in Fig. 2.11. Strain plot contours in (a) for the high-excitation, and, in (b) for the low-excitation are scaled to their maximum amplitudes. This is useful for assessing in-plot patterns across low and high excitation amplitudes. Strain values in the high-excitation case were on average an order of magnitude higher but even then they were much smaller than operational levels. Despite that and despite overall similarity between the two cases, there are nontrivial features emerging in the high-excitation case that are not present in the low-excitation case. In particular, left-hand edges of middle and right modes in row (a) now feature strain hotspots that are absent from corresponding shapes in (b). It would be interesting to see how these variations evolve as the strain amplitudes approach those of the operating environment. This will be explored in future studies where the variations will also be numerically quantified.

2.6 Concluding remarks

A detailed study is presented where full-field non-contact surface strains are measured and integrated into simulation environment using advanced measurement and analysis techniques. This was demonstrated on a number of real engine hardware as well as for a wide dynamic range spanning from low frequency fundamental modes to high frequency complex modes.

Through careful post-processing and integration with simulation results, it has been shown that assessment of design intent can be effectively done using directly acquired full-field non-contact strain measurements. Traditionally displacements are measured and correlated in this manner as they are the most readily accessible quantities. The main objective inevitably is to get a handle on stresses and strains as they are the ultimate parameters used in assessment of the structural integrity. The ability to measure and then perform quantified correlation of strains directly is a major achievement and a step change from existing established practices.

Utilising existing modal analysis correlation metrics, not only the overall degree of similarity but also the coordinate specific contributions were quantified. A remarkable degree of match was obtained between measured and predicted strain mode shapes both visually and numerically. By repeating the measurements at low and high excitation levels, vibration amplitude dependence of strain mode shapes was evaluated. It is important to note that some of the changes were distributed and as such would not have been possible to capture with use of discrete strain measurement means (e.g. SGs).

Although on average the degree of correlation obtained was high, there were some modes where this was markedly low. There are a number of reasons. Some of them have to do with the discrepancies in representation of physics between the test and the simulation environments. Boundary conditions and interactions at these boundaries together with variations in actual and simulated geometries and alignment errors between test and FE coordinates were contributing factors.

This study will be expanded to account for these shortcomings. First of all more blades will be tested to form a statistical understanding. Reverse engineered FE models for each blade will be created by geometry scanning their actual hardware. This will significantly reduce uncertainties introduced due to mass and stiffness distribution discrepancies. Care will be

taken to get simulation models to replicate test boundary conditions more faithfully rather than using idealised constraints. In addition, alignment process performed to match test points with FE nodes will be improved considerably to eliminate artificial errors introduced with the existing method.

Acknowledgements The authors are grateful to Rolls-Royce plc for allowing the publication of this work.

References

1. Pedrini, G., Tiziani, H.J.: Double pulse electronic speckle interferometry for vibration analysis. Appl. Opt. **33**, 7857–7863 (1994)
2. Pedrini, G., Froning, P., Fessler, H., Tiziani, H.J.: Transient vibration measurements by using multi-pulse digital holography. Opt. Laser Technol. **29**(8), 505–511
3. Stanbridge, A.B., Martarelli, M., Ewins, D.J.: Scanning laser Doppler vibrometer applied to impact modal testing. Shock Vib. Digest. **32**, 35 (2000)
4. Beberniss, T.J., Ehrhardt, D.A.: High-speed 3D digital image correlation vibration measurement: Recent advancements and noted limitations. Mech. Syst. Signal Process. (2016). doi:10.1016/j.ymssp.2016.04.014
5. Vuye, C., Vanlanduit, S., Preseznia, F., Steenackers, G., Guillaume, P.: Optical measurement of the dynamic strain field of a fan blade using a 3D scanning vibrometer. Opt. Lasers Eng. **49**, 988–997 (2011)
6. Maguire M., Sever I. A.: Full-field strain measurements on turbomachinery components using 3D SLDV Technology. AIVELA conference, 28 June–1 July 2016, Ancona, Italy
7. Sever, I. A: Experimental validation of turbomachinery blade vibration predictions. Ph.D. thesis, Imperial College London (2004)
8. Kammer, D.C.: Sensor placement for on-orbit modal identification and correlation of large space structures. J. Guid. Control. Dyn. **14**(2), 251–259 (1991)
9. Cazzolato, B., Wildy, S., Codrington, J., Kotousov, A., Schuessler, M.: Scanning laser vibrometer for non-contact three-dimensional displacement and strain measurement. In: Proceedings of Acoustics 2008, 24–26 November 2008, Geelong, Australia (2008)
10. Polytec, "Polytec data sheet – Optical Measurement of Dynamic Stress and Strai", Waldbronn: Polytec (2011)
11. Polytec, "Importance of Video Triangulation for the PSV-3D Scanning Vibrometer", Application note VIB-G-19, (2010)
12. Ewins, D. J.: Modal Testing: Theory, Practice and Application, 2nd edn. Research Studies Press, Baldock (2000)
13. Polytec user manual – Vibrometer controller OVF 5000

Chapter 3
Nonlinear Prediction Surfaces for Estimating the Structural Response of Naval Vessels

Alysson Mondoro, Mohamed Soliman, and Dan M. Frangopol

Abstract Structural health monitoring (SHM) of naval vessels is essential for assessing the performance of the structure and the fatigue damage accrued over the service life. The direct integration of available SHM data may be useful in reducing the epistemic uncertainties arising from inaccuracies in the modeling and the variations in the as-built structural configuration from the initial design. Based on SHM data, fatigue damage indices can be predicted by implementing cell based approaches, such as the lifetime weighted sea method, that discretizes the operational conditions of the vessel into cells with specific wave height, heading angle, and speed. The integration of SHM data into the fatigue assessment using lifetime weighted sea method requires a complete set of data that covers the whole operational spectrum. However, technical malfunctions or discrete monitoring practices generate incomplete data sets. This paper proposes nonlinear prediction surfaces to estimate the ship structural response in unobserved cells based on available cell data. Expected theoretical variations of the structural response to changes in wave height, heading angle, and vessel speed are integrated in the development of the prediction surface. The proposed methodology is illustrated on the SHM data from a high speed aluminum catamaran.

Keywords Fatigue • Aluminum vessels • Structural health monitoring • Missing data • Nonlinear prediction

3.1 Introduction

SHM data can aid in the life-cycle management of structures by helping to identify the discrepancies between predicted and observed performance. The recorded SHM data provides an indication of the as-built condition of the ship and any variations in observed response from anticipated design conditions [1]. In both civil and marine structures, SHM data can be used to update design estimates for expected loads, structural responses, and fatigue life evaluation [2–5]. Fatigue cracking is a major concern in the life-cycle management of naval vessels. The constant fluctuations in loading, induced by the natural variability in sea surface, contributes to damage accumulation in fatigue sensitive details. If the observed conditions deviate substantially from their predicted values, fatigue damage may be either (a) significantly less than expected and lead to unnecessary and costly inspections, or (b) significantly higher than expected and may induce catastrophic failure with high consequences.

The lifetime weighted sea method, used to assess the fatigue life, is developed around the assumption that the operational condition can be discretized into cells where the response in each cell is stationary [6]. A cell is defined by a set of operational conditions which include wave height, ship speed, and heading angle. The total response is the summation of the response in each cell weighted by the probability of occurrence of the cell [7]. The prediction of fatigue life thus requires information to be available for all cells.

Missing data is a problem inherent in the use of SHM for fatigue analysis. First, discrete monitoring practices, while useful in limiting financial costs [8], can lead to some operational states (i.e., cells) not being recorded. Second, technical malfunctions can result in missing or unreliable data [9]. Lastly, even if data is recorded for all cells in the current operational theatre, the future operational conditions may not be similar to past ones; thus, there may be cells in the future profile that can be considered as missing data. Zhu [10] and Mondoro et al. [11] have begun to address the problem of missing data with respect to the structural response characterization of naval vessels. Linear surfaces were used to relate the operational

A. Mondoro • D.M. Frangopol (✉)
Department of Civil and Environmental Engineering, ATLSS Engineering Research Center,
Lehigh University, 117 ATLSS Dr., Bethlehem, PA 18015-4729, USA
e-mail: Dan.frangopol@lehigh.edu

M. Soliman
School of Civil and Environmental Engineering, College of Engineering, Architecture and Technology,
Oklahoma State University, 207 Engineering South, Stillwater, OK 74078-5033, USA

R. Barthorpe et al. (eds.), *Model Validation and Uncertainty Quantification, Volume 3*,
Conference Proceedings of the Society for Experimental Mechanics Series, DOI 10.1007/978-3-319-54858-6_3

conditions (i.e. wave height, ship speed, and heading angle) to a structural response characteristic. The linear surface is useful for the ease of implementation. Additionally, it requires only a minimal amount of prediction model parameters to be estimated which limits the variations that arise based on availability of data. However, the linear surfaces lack a theoretical foundation.

This paper proposes a nonlinear surface for use in predicting unobserved data. The prediction is based on the theoretical relationship between operating conditions and the structural response given as a function of the vertical bending moment. Available data is discretized into cells, the low and high frequency content are separated and fit with response parameters as detailed in [11], and the goodness-of-fit of the theoretically-based nonlinear prediction surface is evaluated and compared with that of the linear surface. Furthermore, the performance of the theoretically-based nonlinear prediction surface is evaluated for several cases with different percentage of missing data. The methodology is applied to the SHM data obtained during the seakeeping trials of the HSV-2 Swift.

3.2 Available Data and Analysis

The full stress time-history of a structural detail is a nonstationary random process due to the exposure to various loading conditions associated with sea states, routes, and speeds. However, the full stress time-history response can be discretized into cells based on wave height H_s, ship speed V, and heading angle β [6]. This discretization leads to stationary processes for the stress time-history in each cell, for which the response spectrum can be estimated. Mondoro et al. [11] proposed that the SHM response spectrum can be fit with functional forms developed from wave spectra. The low and high frequency components were fit separately in order to account for the following actions: wave loads for low frequency, and slamming for high frequency. The Pierson-Moskowitz wave spectrum and the Joint North Sea Wave Observation Project (JONSWAP) were included as two representative wave spectra. The generalized variations of the Pierson-Moskowitz spectrum and the JONSWAP spectrum take the form [11]

$$S^{+}_{PM_{GEN}}(\omega) = \frac{A_{LF}}{\omega^5} e^{-B_{LF}\omega^{-4}} + \frac{A_{HF}}{\omega^5} e^{-B_{HF}\omega^{-4}} \tag{3.1}$$

$$S^{+}_{JONSWAP_{GEN}}(\omega) = \frac{C_{LF}}{\omega^5} \exp\left(-\frac{5}{4} {D_{LF}}^4 \omega^{-4}\right) {E_{LF}}^{\exp\left(-\frac{(\omega - D_{LF})^2}{2{D_{LF}}^2\sigma^2}\right)} + \frac{C_{HF}}{\omega^5} \exp\left(-\frac{5}{4} {D_{HF}}^4 \omega^{-4}\right) {E_{HF}}^{\exp\left(-\frac{(\omega - D_{HF})^2}{2{D_{HF}}^2\sigma^2}\right)} \tag{3.2}$$

where A_{LF} and B_{LF} are fitting parameters for the low frequency content and A_{HF} and B_{HF} are fitting parameters for the high frequency content of the complete generalized Pierson-Moskowitz function, $S^{+}_{PM_{GEN}}$; and C_{LF}, D_{LF}, and E_{LF} are the fitting parameters for the low frequency content and C_{HF}, D_{HF}, and E_{HF} are fitting parameters for the high frequency content of the complete generalized JONSWAP function,$S^{+}_{JONSWAP_{GEN}}$.

3.3 Development of Theoretical Prediction Surfaces

Discrete monitoring practices and technical malfunctions contribute to the missing data problem inherent in SHM. This presents a significant challenge in the fatigue analysis of naval vessels, which is dependent on complete data sets. Linear prediction surfaces have been employed in [10, 11] to relate structural response to wave height, ship speed, and heading angle. The linear prediction surface, Ψ^{lin}, is defined as

$$\Psi^{lin} = p_1 H_s + p_2 V + p_3 \cos(\beta) \tag{3.3}$$

where H_s is the wave height, V is the ship speed, and β is the heading angle. The linear surface is included in this paper for comparison purposes. The following subsections present the development of the theoretically-based nonlinear prediction surfaces. The discussion is framed around the HSV-2 Swift but is readily applicable to other naval vessels.